Analytica Chimica Acta 1008 (2018) 38–47

Contents lists available at ScienceDirect

Analytica Chimica Acta

journal homepage: www.elsevier.com/locate/aca

Synthesis of gold-palladium nanowaxberries/dodecylamine-functionalized graphene quantum dots-graphene micro-aerogel for voltammetric determination of peanut allergen Ara h 1

Ruiyi Li [a], Ling Liu [a], Haiyan Zhu [a], Zaijun Li [a, b, *]

[a] School of Chemical and Material Engineering, Jiangnan University, Wuxi, 214122, China
[b] Key Laboratory of Synthetic and Biological Colloids, Ministry of Education, Wuxi, 214122, China

HIGHLIGHTS

- Graphene micro aerogel was synthesized by using a Pickering emulsion as the template.
- New seed growth method was developed for fabrication of gold-palladium nanowaxberries.
- Hybrid of AuPd nanocrystals, graphene quantum dots and graphene micro-aerogel was made.
- The hybrid offers unique three-dimensional architecture and excellent electrocatalytic activity.
- The DNA sensor based on hybrid exhibits the best sensitivity for detection of DNA up to now.

GRAPHICAL ABSTRACT

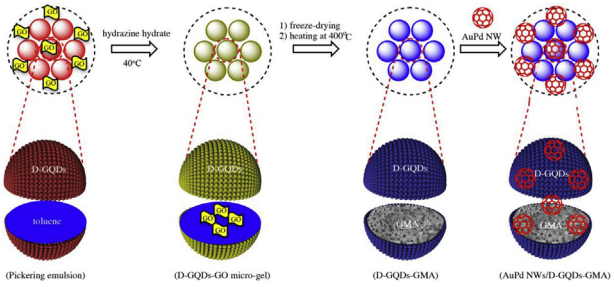

ARTICLE INFO

Article history:
Received 31 October 2017
Received in revised form
7 January 2018
Accepted 15 January 2018
Available online 30 January 2018

Keywords:
Hybrid
DNA biosensor
Electrocatalysis
Peanut allergen Ara h 1
Peanut milk beverage

ABSTRACT

The paper reports synthesis of gold-palladium nanowaxberries(AuPd NWs)/dodecylamine-functionalized graphene quantum dots(D-GQDs)-graphene micro-aerogel(GMA). D-GQDs was used as a solid particle surfactant for stabilizing Pickering emulsion of toluene-in-graphene oxide aqueous dispersion. Graphene oxide sheets in the aqueous phase are reduced by hydrazine hydrate, diffused into the toluene droplet and self-assembled into graphene oxide micro-gels. Followed by freeze-drying, thermal annealing and hybridized with AuPd NWs. The as-prepared AuPd NWs/D-GQDs-GMA shows an unique three-dimensional structure with the size of microns. The small size and strong polarity make it can be directly dispersed in ethanol to form stable dispersion for sensor preparation. The hybrid of GMA, D-GQDs and AuPd NWs greatly improves the electron transfer, electroactive surface area and ion diffusion. The architecture of conductor/semiconductor/conductor achieves to a significant amplification of detection signal. The DNA biosensor based on the AuPd NWs/D-GQDs-GMA exhibits ultrasensitive differential pulse voltammetric (DPV) response towards peanut allergen Ara h 1. The DPV signal linearly increases with increasing DNA concentration in the range of 1.0×10^{-22}-1.0×10^{-17} M with the detection limit of 4.7×10^{-23} M (S/N = 3). The analytical method was successfully applied to voltammetric determination of peanut allergen Ara h 1 in peanut milk beverage.

* Corresponding author. School of Chemical and Material Engineering, Jiangnan University, Wuxi, 214122, China.
E-mail address: zaijunli@jiangnan.edu.cn (Z. Li).

https://doi.org/10.1016/j.aca.2018.01.031
0003-2670/

1. Introduction

Peanut allergy has a worldwide prevalence of 0.5–2% that appears to be increasing [1]. The symptoms of peanut allergy range from mild oral allergy syndrome to anaphylactic reactions, and even death. The therapy for peanut allergy only focuses on primarily peanut avoidance, early recognition of symptoms brought by accidental ingestion and pharmacologic treatment of the adverse reactions [2]. The development of rapid and convenient analytical methods for food allergen is extremely desirable.

A large number of analytical techniques have been developed for the detection of DNA including dynamic light scattering [3], electrochemiluminescence [4], surface-enhanced Raman spectroscopy [5], phosphorescence resonance energy transfer [6], quartz crystal microbalance [7], colorimetry [8], fluorescence [9] and electrochemistry [10]. The electrochemical sensors have attracted particular attention due to their easy operation, rapid response, low cost, high sensitivity and selectivity [11]. However, there is a great challenge in the efficiency and sensitivity of signal amplification for electrochemical sensor design. The main amplification strategies for electrochemical sensors are the nanomaterial-based amplification [12], nonlinear hybridization chain reaction [13], circular strand displacement polymerization and hyperbranched rolling circle amplification [14], ligase chain reaction [15] and rolling circle amplification [16]. The assays with enzyme often are sensitive to temperature, pH, salt and toxic chemicals, thus the nanomaterial based amplification strategies have paid more attention. Many nanomaterials have been explored and synthesized for non-enzyme DNA biosensors such as noble metal nanoparticles [17,18], polymethylene Blue [6], carbon nanotubes [19] and graphene [20]. Noble metal and graphene are the most frequently used for the construction of electrochemical sensors due to their excellent electrocatalytic activity. The hybrid of noble metal and graphene become a hot research topic in material science, because the hybrid potentially paves one way to improve their electronic, chemical and electrochemical properties [21]. The investigations have demonstrated that noble metal-graphene can offer a much better electrocatalytic activity compared with single noble metal nanoparticles and single graphene. To improve the electrochemical property, our group developed one gold-graphene hybrid [22]. The hybrid is composed of high density graphene aerogel (HDGA) and gold nanostars (GNSs). Compared with previously reported noble metal-graphene hybrids, the GNSs-HDGA exhibits a much better structural stability and electrocatalytic activity [23]. However, there still is deficiency when it is used as the sensing material for DNA biosensors. On the one hand, the GNSs-HDGA has to be crushed into tiny powder before its use because the sensor preparation mostly requires the use of tiny powder material rather than large size of graphene aerogel. However, the tearing may destroy the characteristic structure of graphene hydrogel and lead to the partial loss of electronic and mechanical properties of the pristine graphene aerogel. On the other hand, the combination between hydrophobic HDGA and hydrophilic GNSs in the hybrid is loose due to their weak interaction. Due to lack of intimate chemical and electrical contacts, such a hybrid is difficult to achieve a significant synergy in electrochemistry between HDGA and GNS. In addition, the HDGA is highly hydrophobic. The hydrophobic characteristic of HDGA makes hydrophilic electrolyte is difficult to approach the electrode surface. This leads to a slow electrochemical response process. The existence of above problems greatly limits its application in electrochemical fields.

In the study, we report synthesis of gold-palladium nanowaxberries (AuPd NWs)/dodecylamine-functionalized graphene quantum dots(D-GQDs)-graphene micro-aerogel(GMA). The hybrid material shows excellent electrocatalytic activity towards $Fe(CN)_6^{4-}$. It has been successfully applied as a sensing material to voltammetric determination of peanut allergens Ara h 1.

2. Experimental

2.1. Materials and reagents

Graphene oxide (GO) was prepared by the Hummers' method [24]. The D-GQDs were synthesized via thermal pyrolysis of citric acid and dodecylamine in ammonium hydroxide solution [25]. The TE buffer solution contained 10 mM Tris-HCl and 1 mM EDTA (pH 8.0). The phosphate-buffered saline (PBS, pH 7, Na_2HPO_4-KH_2PO_4-NaCl-KCl, 0.01 M) was prepared in the laboratory. Oligonucleotides 1 (probe DNA, 5′-HS-C6-GCG AGG TTC CGT GGC TGC TGA TGA CTT GGT CCT CGC-biotin-3′), oligonucleotides 2 (target DNA, 5′-ACC AAG TCA TCA GCA GCC ACG GAA-3′), Oligonucleotides 3 (single mismatch, 5′-ACC AAG TAA TCA GCA GCC ACG GAA-3′), and oligonucleotides 4 (non-complementary, 5′-GTT CGA CTG CTG ATG ATT GTA AGG-3′) were purchased from Sangon Biotech Co., Ltd. (Shanghai, China). The loop sequence of the probe is the conserved sequence of Ara h 1-main allergen of peanut.

2.2. Material characterization

Scanning electron microscope (SEM) was carried out in a HITACHI S4800 field emission scanning electron microscope. SEM sample was prepared by placing a drop of dilute ethanol dispersion of the composites onto a copper plate attached to an aluminum sample holder, and the solvent was allowed to evaporate at room temperature. Transmission electron microscope (TEM) analysis was conducted on a JEOL 2010 transmission electron microscope at 200 keV. The sample was prepared by dispensing a small amount of dry powder in ethanol. Then, one drop of the suspension was dropped on 300 mesh copper. TEM grids covered with thin amorphous carbon films. X-ray diffraction (XRD) patterns were measured on an X-ray D8 Advance Instrument operated at 40 kV and 20 mA and using Cu Kα radiation source with $\lambda = 0.15406$ nm. Infrared spectrum (IR) was recorded on a Nicolet FT-IR 6700 spectrometer. Raman measurements were carried out using an InVia laser micro-Raman spectrometer. The optical microscopy images of emulsion were recorded using a VHX-1000C Shooting optical microscope (Kean Co. Ltd, Hongkong in China). N_2 adsorption and desorption isotherms were measured at 77 K on a Quantachrome Nova 2000. Prior to the gas sorption measurements, all the samples were outgassed in vacuum at 120 °C for 24 h. The specific surface area and the pore size distribution were calculated using the Braunauer-Emmett-Teller (BET) method and the relative pressure range of p/p_0 from 0.1 to 0.3 was used for multipoint BET calculations. Non-local density functional theory assuming the pores are slit/cylinder shaped was used to determine the pore size distribution and mesopore volume. Electronic conductivity measurement was carried out in a ST-2258C multifunction digital four-probe tester which equipped with a SZT-D semiconductor powder resistivity tester (Suzhou Jingge Electronic Co., Ltd., China). The powder sample was directly placed in a round hole with the diameter of 5 mm on the SZT-D semiconductor powder resistivity tester. Then, the powder was slowly compressed by the piston on

the system. At the same time, the electronic conductivity values under different pressures were automatically recorded.

2.3. AuPd NWs preparation

The $HAuCl_4$ solution (10 ml, 12 mM) was mixed with the citrate acid solution (8.0 ml, 0.15 M) containing tannic acid (0.36 M) in a glass vial and then heated at 80 °C until it turned into clear crimson. The temperature was rapidly raised to 100 °C, maintained for 6 min and then cooled in air to room temperature to obtain gold seed solution. In another glass vial, the $HAuCl_4$ solution (0.1 ml, 30 mM) and the H_2PdCl_4 solution (0.1 ml, 30 mM) were mixed with the citrate acid aqueous solution (10 ml, 5 mM) and then incubated for 5 min under stirring at 1000 rpm. The gold seed solution (0.05 ml) was rapidly injected into the above mixed solution after added the $AgNO_3$ solution (0.15 ml, 0.01 M) and H_2O_2 (10 ml, 30%). After about 30–40s, the stirring was stopped. The obtained AuPd NW solution was stored in a refrigerator at 4 °C before use.

2.4. AuPd NWs/D-GQDs-GMA preparation

D-GQDs (100 mg) were dissolved in the GO aqueous dispersion (30 ml, 10 mg ml^{-1}) in a beaker (100 ml). Added toluene (30 ml) into the above dispersion and then stirred for 20 s at 13000 rpm on a HN-30K handheld homogenizer (Shanghai HANUO Instrument Co. Ltd, China) to form a toluene-in-water emulsion. Added hydrazine hydrate (0.5 g) into the above emulsion and heated at 40 °C for 6 h. Followed by freeze-drying and thermal annealing in Ar/H_2 at 400 °C for 4 h to obtain the D-GQDs-GMA. In another glass vial, the part of D-GQDs-GMA sample (0.5 g) was dispersed into the AuPd NWs solution. The solution was rapidly sucked into D-GQDs-GMA and then dried by freeze-drying to obtain the AuPd NWs/D-GQDs-GMA.

2.5. DNA-biosensor fabrication

The AuPd NWs/D-GQDs-GMA in ethanol (0.4 mg ml^{-1}, 5 μl) was dropped on the GCE surface and dried in air. After the chitosan solution (1% (w/v), 2 μl) was spread on the sensing material surface and dried in air, the probe DNA (1.0×10^{-6} M, 10 μL) was dropped on the modified GCE surface and dried at room temperature. To remove unfixed probe DNA, the ssDNA-biosensor was rinsed with TE buffer and ultrapure water for three times. Before use, the as-prepared ssDNA-biosensor was stored in a refrigerator at 4 °C. To prepare dsDNA-biosensor, the ssDNA-biosensor was immersed into 2 × SSC buffer solution containing target DNA for 30 min at 37 °C. Then, it was rinsed with 0.5% SDS and deionized water respectively to remove the unbound target DNA.

2.6. Electrochemical measurements

The electrochemical measurement was performed with CHI660D electrochemical workstation (Shanghai, China). Conventional three electrode system was used for cyclic voltammetry (CV) with Ag/AgCl (saturated KCl) electrode as the reference electrode, platinum wire as the counter electrode, and bare or modified GCE electrode as the working electrode. Before use, glassy carbon electrode (GCE, 1.0 mm in diameter) was polished successively with 1.0, 0.3, and 0.05 μm alumina powder, and sonicated in a 6.0 M of nitric acid/doubly distilled water and ethanol/doubly distilled water for 20 min. The GCE was subjected as working electrode to cyclic scanning in 0.5 M sulphuric acid solution in a potential range from −0.1 V to 1.0 V. When the cyclic voltammogram was almost unchanged, the electrode was taken out, cleaned with ultra pure water and finally dried in stream of nitrogen. The electrochemical experiments were carried out under room temperature and all experimental solution was degassed by nitrogen for at least 15 min. The nitrogen atmosphere was maintained during electrochemical measurement. The cyclic voltammogram (CV), differential pulse voltammogram (DPV) and electrochemical impedance spectroscopy(EIS) were measured in PBS of pH 7 containing 1.0 mM $K_4Fe(CN)_6$. For EIS measurement, the potential amplitude of ±5 mV and a frequency range of 0.01–105 Hz were adopted. The reported result for every electrode was the mean value of five parallel measurements.

2.7. Peanut DNA extraction from peanut milk beverage

Peanut milk beverage was purchased from the supermarket in Wuxi city and its peanut DNA extraction was completed by using a reported procedure [26,27]. In a typical extraction, 5 mL of the sample was centrifuged at 3000 rpm and 4 °C for 10 min. Discarded the supernatant and rubbed out the lipid by absorbent cotton. Then, added 10 mL of the PBS of pH 7 to dissolve the sediment. The last step was repeated for three times. Discarded the supernatant and rubbed out the lipids. Then, an extraction buffer (0.2 M Tris-HCl, pH 7.5, 0.25 M NaCl, 25 mM EDTA, 0.5% SDS) was added to dissolve the pellet and incubated at 60 °C for 30 min. Then, 100 μL of cold phenol/chloroform/isoamyl alcohol (25:24:1) was added. Followed by the centrifugation at 12000 rpm and 4 °C for 10 min. Then, 200 μL of pre-cooling isopropyl alcohol was added to the supernatant and incubate at −20 °C for 20 min. After the centrifugation at 12000 rpm and 4 °C for 10 min, 150 μL of ethanol was added to wash the pellet. The supernatant was discarded and the pellet was re-suspended by adding 50 μL of micro-filtered water.

3. Results and discussion

3.1. Material design

Our design is to build a highly sensitive sensing material for voltammetric determination of DNA. In the AuPd NWs/D-GQDs-GMA, different component plays different roles. The GMA serves as a conductor. Its high electron conductivity leads to a fast electron transfer. In addition, the GMA also serves as a scaffold. Its large specific surface gives abundant binding sites for D-GQD, and open porous structures offers a high electrolyte transport rat. The AuPd NW serves as another conductor. Its high electron conductivity speeds up the electron transfer. In addition, the AuPd NW also serves as a catalyst. Its unique structure achieves to a high electrocatalytic activity towards $Fe(CN)_6^{4-}$. The D-GQD serves as a semiconductor. The characteristics of p-type semiconductor makes it gives an effective carrier migration. In addition, the D-GQD also serves as a linker. Its hydrophobic alkyl chains are firmly fixed at the GMA surface during the formation of D-GQDs-GMA. The hydrophilic groups can strongly interact with the chemically active groups and atoms of AuPd NWs due to their good affinity. The action achieves to an effective connection of GMA, D-GQD with AuPd NW. The connection greatly accelerates the electron and energy transfer between different components in the hybrid. More importantly, our design creates an architecture of conductor/semiconductor/conductor. The architecture is similar with the Schottky Barrier Diode (SBD) [28]. The SBD is a powerful tool for amplifying electrical signals, thus the architecture of AuPd NWs/D-GQDs-GMA brings an enhanced electrochemical response towards $Fe(CN)_6^{4-}$.

3.2. Material synthesis

Synthesis of the AuPd NWs/D-GQDs-GMA includes the

preparation of D-GQDs-GMA and AuPd NWs as well as their hybridization (see Fig. 1). First, Pickering emulsion of toluene-in-GO aqueous dispersion was made by using the D-GQDs as the solid particle surfactant. Due to high surface activity, the Pickering emulsion stabilized by D-GQDs has high stability. In the emulsion system, the D-GQDs were assembled on the interface of toluene/water, and GO sheets were dispersed in the aqueous phase, not in the toluene droplets due to their high hydrophilicity. Fig. s1 indicates that the toluene droplets in the emulsion are regular spheres with a relatively wide size distribution. Next, the amounts of hydrazine hydrate was added into the Pickering emulsion to reduce GO sheets. Due to rapid decrease in polarity with reducing GO sheets, GO sheets will slowly diffuse into the interior of toluene droplets driven by water molecules and self-assembled in the interior of toluene drops, finally resulting in the formation of D-GQDs-GO micro-gel. In the step, the reaction temperature was seriously controlled at 40 °C. A relatively low and constant temperature bring a slow and constant reduction rate for GO sheets. This ensures that the final graphene aerogel contains a denser and finer graphene framework networks compared with the classical graphene aerogel. Further, the D-GQDs-GO micro-gel was treated by freeze-drying and thermal annealing in N_2 at 400 °C to obtain D-GQDs-GMA. During the thermal annealing, chemically active groups were stripped from the edge of GO sheets. However, the use of too high temperature for the annealing may seriously destroy the functional structure and groups in the D-GQDs. This may lose many catalytic active sites come from the D-GQDs. Thus, a moderate temperature, 400 °C, was selected for thermal annealing.

Fig. s2 shows that the D-GQDs-GMA is composed of small graphene aerogels with the size of microns. Small size and high polarity makes it easy to be dispersed in ethanol or other organic solvents to form stable dispersion for sensor preparation (see Fig. s3). Thus, any tearing or grinding of graphene aerogel sample is not required before the sensor preparation. This direct dispersion not only brings the convenience for sensor preparation and good reproducibility of the batch production but also can maintain the integrity of original graphene aerogel structure that preserves the excellent electrochemical properties. Compared with common graphene aerogel, the D-GQDs-GMA also indicates a denser and finer graphene framework networks. The structural characteristic improves the electronic conductivity, specific surface and structural stability.

The AuPd alloy was made by one new seed growth method. Fig. s4 shows that the AuPd alloy gives a waxberry-like nanostructure with the average particle size of 81.2 nm that consists of tiny AuPd nanocrystals of less than 5 nm. The special structure is attributed to the use of tannic acid as the stabilizer. Tannic acid is a polyphenolic compound, its use realizes the interconnection between AuPd nanoparticles during the growth of AuPd crystals. The interconnection effectively reduces the distance between AuPd nanocrystals and leads to a high electronic conductivity. The small size of AuPd nanocrystals makes the Au and Pd atoms in the alloy be fully exposed outside. This increases the opportunity that Au and Pd atoms in the alloy participate in the catalysis. In addition, the spiny surface of AuPd nanocrystals brings a much stronger localized Surface Plasmon Resonance compared with the AuPd alloys with the smooth appearance, which has been verified by the result of surface enhanced Raman scattering analysis in Fig. s5.

The D-GQDs-GMA was dispersed in the AuPd NW aqueous solution and then dried by freeze-drying to obtain AuPd NWs/D-GQDs-GMA.

3.3. Structural characterization

The AuPd NWs/D-GQDs-GMA was characterized by SEM, TEM, XRD pattern, FTIR spectrum and Raman spectrum technologies. Fig. 2 indicates that the hybrid has a three-dimensional architecture with the rich of open pores. On the XRD pattern there are nine XRD diffraction peaks at 26°, 38.28°, 39.80°, 44.48°, 46.34°, 64.6°, 67.88°, 77.64°and 81.57°. The peak at 26° is assigned to graphene, corresponding to the crystal plane (002) of graphene. The peaks at 39.80°, 46.34°, 67.88° and 81.57° are assigned to Pd nanocrystals, corresponding to crystal planes Pd (111), Pd (200), Pd (220) and Pd (311) of Pd face-centered cubic structure. The peaks at 38.28°, 44.48°, 64.6° and 77.64° are assigned to Au nanocrystals, corresponding to crystal planes Au (111), Au (200), Au (220) and Au (311) of Au face-centered cubic structure. On the IR spectrum there are several IR absorption peaks and bands. Since chemically active groups have been fully stripped from the GO sheets during the thermal annealing, thus the IR absorptions are mainly attributed to the D-GQDs in the hybrid. The band at between 3600 cm^{-1} and 3300 cm^{-1} is stretching vibrations of the O-H and N-H bonds. The peak at 1689 cm^{-1} is stretching vibration of the -C=O bond. The peak at 1390 cm^{-1} is stretching vibration of the C-H group. The peak at 1160 cm^{-1} is stretching vibration of the C-O bond. The above results were also proved by the results of XPS analysis in Fig. s6. On the Raman spectrum of GMA there are two distinct peaks due to D and G bands at around 1362 and 1612 cm^{-1}. The D band is attributed to an A_{1g} vibration mode of carbon atoms with a double-resonance process in plane terminations of disordered graphite,

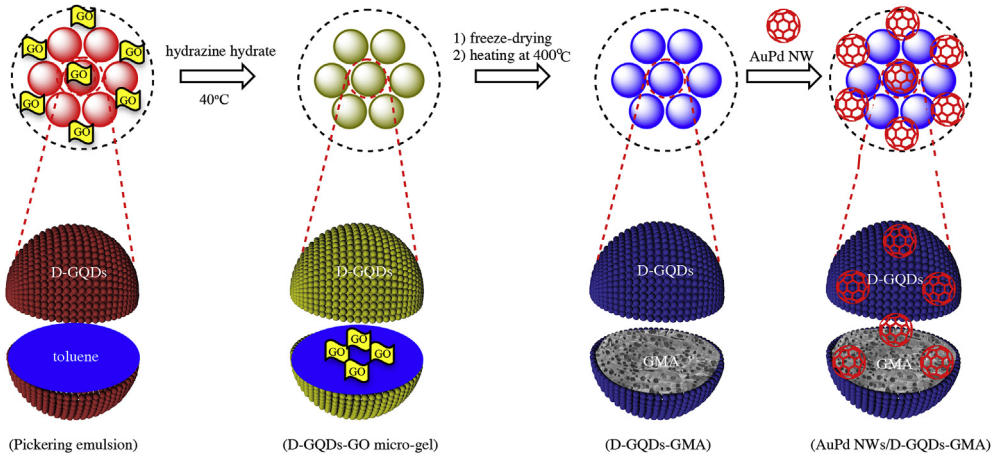

Fig. 1. The procedure for synthesis of AuPd NW/D-GQD-GMA.

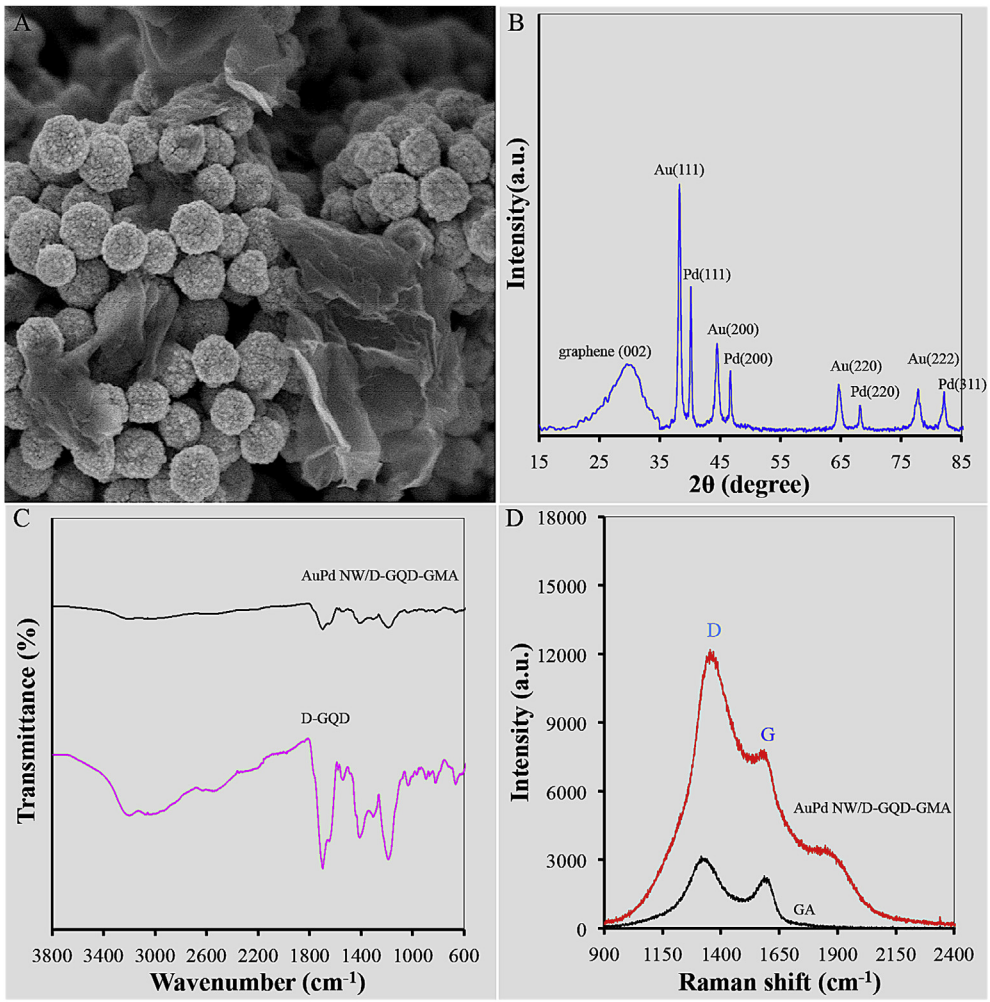

Fig. 2. The SEM image (A), XRD pattern (B), FTIR spectrum (C) and Raman spectrum (D) of AuPd NWs/D-GQDs-GMA.

and G band arises from the E_{2g} mode of graphitic carbon and is assigned to the vibration of sp^2 hybridized carbon atoms in the graphite layer. Fig. 2D also shows that two characteristic Raman peaks of AuPd NWs/D-GQDs-GMA were shifted to 1387 and 1609 cm^{-1}. The G band energy remained virtually unchanged, whereas the D band energy showed a substantial blue-shift of 25 cm^{-1}. Because AuPd NWs have no any Raman absorption at 900-2400 cm^{-1}, the Raman peaks of AuPd NWs/D-GQDs-GMA is contributed to the D-GQDs-GMA. Thus, the result verifies that the energy transfer between the D-GQD and the GMA was achieved in the hybrid. This is analogous to hole doping that has been found to lead to an increase of the D band frequency of graphene [29].

3.4. Electrochemical properties

Fig. 3 presents the CV curves of bare GCE and sensors in a 1.0 mM $K_4Fe(CN)_6$ in the PBS of pH 7. It can be seen that the peak current of GA sensor is higher than that of bare GCE. This is due to large specific surface area and high electron/ion conductivity of the GA. However, the peak current is lower than that of GMA sensor. This is because the GMA has a higher electronic conductivity and larger specific surface area compared with common GA. The higher electron transfer rate and more catalytic sites of GMA leads to a faster electrode reaction process and an increased peak current. The peak current increases when the GMA is replaced by the D-GQDs-GMA. Because most of the surface of GMA is covered with the D-GQDs, the catalytic sites of D-GQDs-GMA are mainly derived from the D-GQDs. The peak current of D-GQDs-GMA sensor is obviously higher than that of D-GQDs sensor (see Fig. s7). The result verifies that the combination of GMA with D-GQDs largely improves the electrochemical response towards $Fe(CN)_6^{4-/3-}$. According to our design, the D-GQDs-GMA offers the architecture of conductor/semiconductor. The architecture is similar with the Schottky Barrier Diode [28]. Thus, the combination speeds up the carrier migration in the semiconductor and results in an obviously electrical signal amplification. After introduced the AuPd NWs, the peak current will continue to increase. The peak current is obviously higher than that of AuPd NWs sensor. Because the catalytic sites of AuPd NWs/D-GQDs-GMA are mainly come from the surface of AuPd NWs, the result also demonstrates that the combination of AuPd NWs with D-GQDs-GMA can enhance the electrochemical response. This is because the combination creates the architecture of conductor/semiconductor/conductor. The carriers in the semiconductor (D-GQDs) are affected by both the conductor (GMA) and its opposite conductor (AuPd NWs), the Schottky Barrier Diode induces a higher electrical signal amplification capability compared with the D-GQDs-GMA.

Fig. 4 presents the CV curves of AuPd NWs/D-GQDs-GMA sensor in a 1.0 mM $K_4Fe(CN)_6$ in the PBS of pH 7 at different scan rates. It can be seen that the value for the peak-peak potential separation

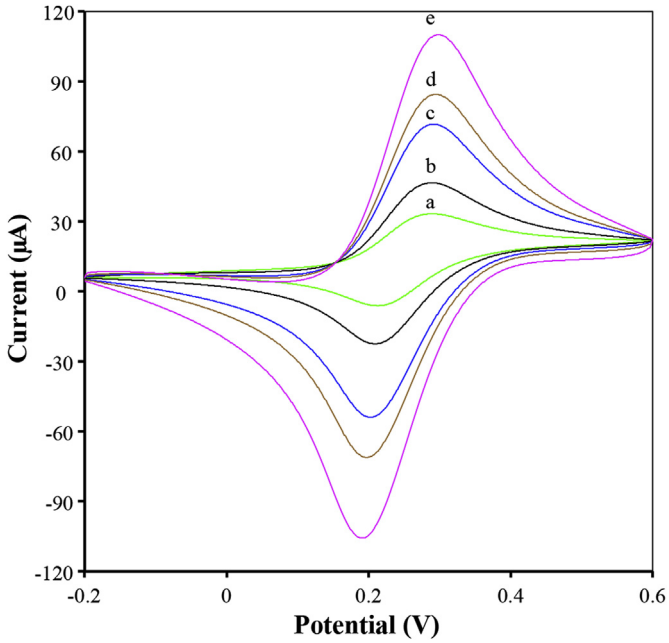

Fig. 3. CV curves of the bare GCE (a) and the sensors based on the GA (b), GMA (c), D-GQDs-GMA (d) and AuPd NWs/D-GQDs-GMA (e) in a 1.0 mM $K_4Fe(CN)_6$ in the PBS at the scan rate of 100 mV s^{-1}.

(ΔE_p) at the scan rates used are very small, indicating a fast electron transfer process between the $Fe(CN)_6^{4-}$ and the electrode. As the $n\Delta E_p$ value is much lower than 200 mV, the apparent heterogeneous electron transfer rate constant (k_s) can be calculated by the Laviron equation in the following [30]: $k_s = mnFv/RT$. The m is a parameter related to the peak-to-peak separation, T is the temperature, n is the number of electrons, and v is the scan rate. The k_s was found to be 19.8 ± 0.32 cm s^{-1} for the AuPd NWs/D-GQDs-GMA sensors. The value is higher than that of the GA sensor (5.92 ± 0.17 s^{-1}), the GMA sensor (8.76 ± 0.12 s^{-1}) and the D-GQDs-GMA sensor (12.76 ± 0.11 s^{-1}), indicating the fastest electron transfer process.

Fig. s8 shows the chronocoulometric cures and Q-$t^{1/2}$ plots of different electrodes in a 1.0 mM $K_4Fe(CN)_6$ in the PBS. The electroactive surface area (ESA) of the sensor was calculated from the slope of the straight line in the corresponding Q-$t^{1/2}$ plot [31]. It was found that the ESA value is 0.0.068 cm^2 for the bare GCE, 0.192 cm^2 for the GA sensor, 0.307 cm^2 for the GMA sensor, 0.516 cm^2 for the D-GQDs-GMA sensor and 0.603 cm^2 for the AuPd NWs/D-GQDs-GMA. From these data, we can see that the ESA value of GA sensor is more than 2-fold that of bare GCE. This is attributed to large specific surface area of the GA. The ESA will increase if the GA was replaced by MGA. This is because the MGA offers a bigger specific surface area and a higher electronic conductivity. Compared with conventional graphene materials, the D-GQDs has a much larger specific surface area due to its small size [32]. The larger surface area brings a more catalytic active sites on the modified layer. Thus, the introduction of GQDs results in an obviously increased ESA. The ESA value will continue to increase after introduced AuPd NWs. This is due to the introduction of new catalytic active sites come from Au and Pd atoms in the AuPd NWs.

Fig. 5 indicates the AC impedance spectra of bare GCE and different sensors in a 1.0 mM $K_4Fe(CN)_6$ in the PBS of pH 7. Based on the equivalent circuit in the inset in Fig. 5, the bulk electrolyte resistance (R_s) and the electron/charge transfer resistance (R_{ct}) were calculated and the results were listed in Table s2. From Table s2, it can be seen that the modification of GA, GMA, D-GQDs or AuPd NWs can cause an obvious reduce in the R_{ct} and leads to an increased electrochemical response towards $Fe(CN)_6^{4-}$. The conclusion was confirmed by the results of CV study. According to the results of electrochemical impedance measurements, the diffusion coefficients of the $Fe(CN)_6^{4-}$ (D) in different modifying layers were also calculated by Levi and Aurbach's equation [33]. It was found that the D value in GMA layer is more than 22.5-fold that in the GA layer. This is due to the high electronic conductivity, large specific surface and good structural stability of GMA. The D value increases if GMA is replaced by D-GQDs-GMA. The D value in D-GQDs-GMA layer is more than 3 times that in GMA layer. Due to good affinity, polar $Fe(CN)_6^{3-/4-}$ ions in the bulk solution are easier to diffuse into polar D-GQDs-GMA layer compared with the hydrophobic GMA layer. This increases the concentration of $Fe(CN)_6^{3-/4-}$ ions in the modified layer. In addition, the spongy D-GQDs layer on the GMA surface works as an ion reservoir to contain the host of the electrolyte, shortening the transport path of $Fe(CN)_6^{3-/4-}$ ions during the electrode reaction. Thus, the introduction of D-GQDs brings an increased D value. The D value will continue to increase after modified with AuPd NWs. This is contributed to high catalytic capacity and electronic conductivity of the AuPd NWs. These factors accelerates the redox of $Fe(CN)_6^{4-}$ on the electrode surface and results in a faster electrode reaction and a higher D value.

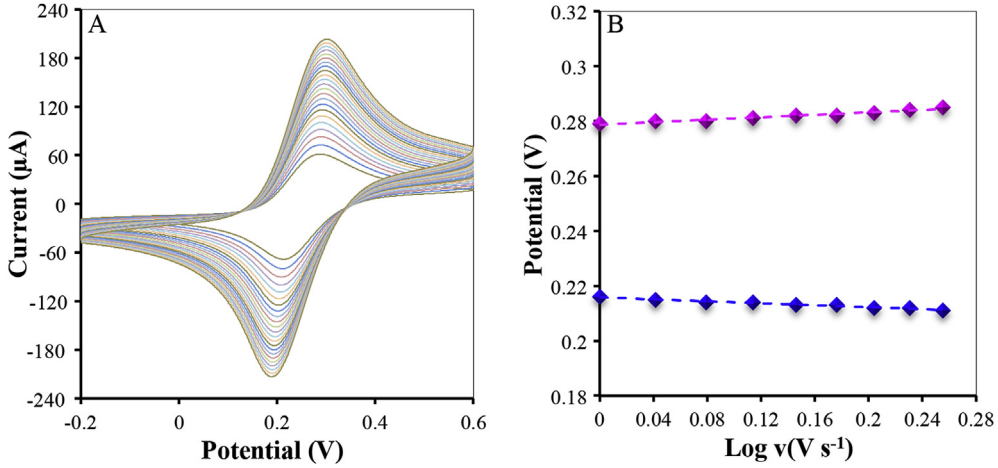

Fig. 4. (A) CV curves of the AuPd NWs/D-GQDs-GMA sensor in a 1.0 mM $K_4Fe(CN)_6$ in the PBS at different scan rates of 0.1, 0.2, 0.3, 0.4, 0.5, 0.6, 0.7, 0.8, 0.9, 1, 1.1, 1.2, 1.3, 1.4, 1.5, 1.6, 1.7, 1.8, 1.9 and 2.0 V s^{-1} and plots of the E_p *vs.* logv (B).

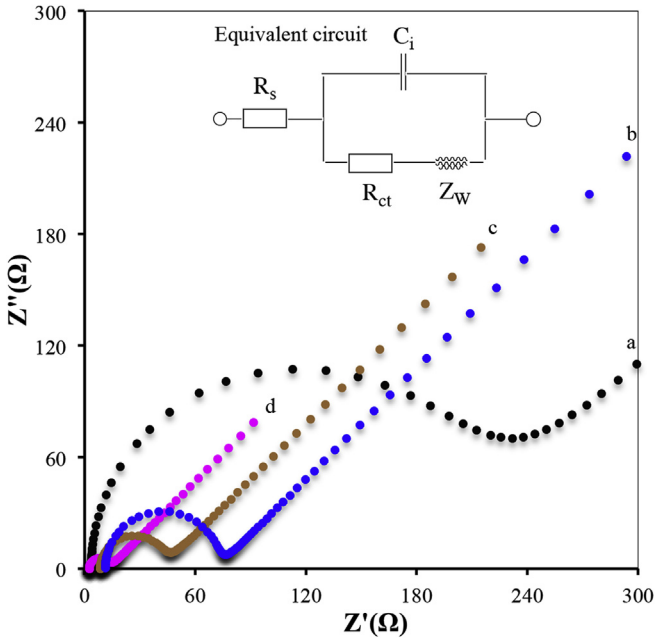

Fig. 5. AC impedance spectra of the sensors based on the GA (a), GMA (b), D-GQD-GMA (c) and AuPd NWs/D-GQDs-GMA (d) in a 1.0 mM $K_4Fe(CN)_6$ in the PBS. Inset: equivalent circuit from the EIS measurements.

3.5. Electrochemical response towards target DNA

To study on the electrochemical response towards target DNA, the CV and DPV behaviors of ssDNA-biosensor and hybridized ssDNA-biosensor with target DNA of 1×10^{-21} M were investigated in a 1 mM $Fe(CN)_6^{4-}$ in the PBS. Fig. 6 indicates that the hybridized ssDNA-biosensor with target DNA offers a higher peak current on the CV curve and DPV curve compared with the ssDNA-biosensor, verifying that the hybridization can bring an increases in the current signal. In addition, Fig. 6 also shows that the change in the DPV signal is obviously bigger than that in the CV signal. Thus, DPV technology was used for detection of peanut allergens Ara h 1.

The sensitive electrochemical response of the ssDNA-biosensor towards target DNA is mainly attributed to the hybridization of probe DNA with target DNA and the interaction between dsDNA and AuPd NWs/D-GQDs-GMA. The early studies have proved that the dsDNA possesses well stacked, nearly parallel bases, with overlapping π-electron system, can be a good candidate for long-range charge transfer [34]. The dsDNA offers a much higher electronic conductivity compared with the ssDNA, thus the hybridization of ssDNA with target DNA will increase the electronic conductivity of the modified layer on the electrode surface. This will accelerate the electron transfer between the $Fe(CN)_6^{4-}$ and the electrode. This leads to a fast electrode reaction process and more sensitive electrochemical response towards $Fe(CN)_6^{4-}$. The increase in the current signal caused by the hybridization is very weak due to the ultra low concentration of target DNA and a relatively poor electronic conductivity of the dsDNA. However, the increase can be greatly amplified by interaction of dsDNA with AuPd NWs/D-GQDs-GMA on the electrode surface. Similar to dsDNA, AuPd NWs/D-GQDs-GMA has a soft three-dimensional structure with the rich of chemically active groups. By the proper structural regulation and strong interaction between their active groups, the surface of AuPd NWs/D-GQDs-GMA is sufficiently close to the surface of dsDNA to form a DNA-based bioconjugate. Due to their intimate chemical and electrical contacts, the combination creates a large overlapping π-electron system. This greatly accelerates the electron transfer rate between the $Fe(CN)_6^{4-}$ and the electrode, leading to a remarkably enhanced electrochemical response.

3.6. Analytical characteristics

Fig. 7 presents the DPV curves of hybridized ssDNA-biosensors with different concentrations of target DNA in a 1.0 mM $Fe(CN)_6^{4-}$ in the PBS. The peak current (I_p) is linear to the concentration of target DNA in the range from 1.0×10^{-22} M to 1.0×10^{-17} M. The corresponding linear regression equations is expressed in the following equation: $I_p = 14.538C + 360$, with statistically significant correlation coefficient of 0.9997, where the I_p is peak current intensity of the oxidization peak in the DPV curve in μA and C is the logarithm value of target DNA concentration in the unit of M. The limit of detection (LOD) was found to be 4.7×10^{-23} M for target DNA that was obtained from the signal-to-noise characteristics of these data (S/N = 3). The sensitivity is much better than that of the reported electrochemical DNA sensors in Table 1.

Repeatability of the ssDNA-biosensor was examined by repeating the DPV measurements around 10 cycles. No significant change was found in the DPV peak current for 10 time measurements, indicating a good repeatability. The ssDNA-biosensor was stored at a dry condition and the temperature of 4 °C for four

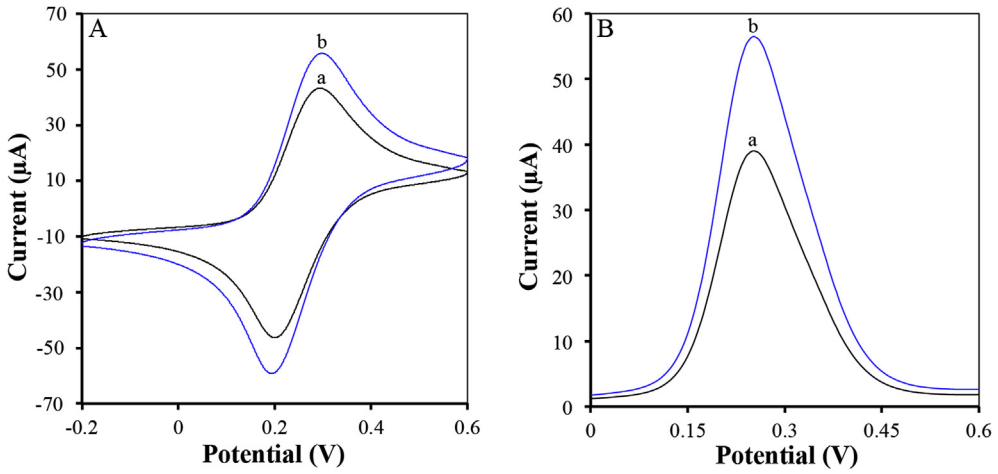

Fig. 6. CV (A) and DPV curves (B) of the ssDNA-biosensor (a) and the hybridized ssDNA-biosensor with the target DNA of 1×10^{-21} M (b) in a 1 mM $K_4Fe(CN)_6$ in the PBS.

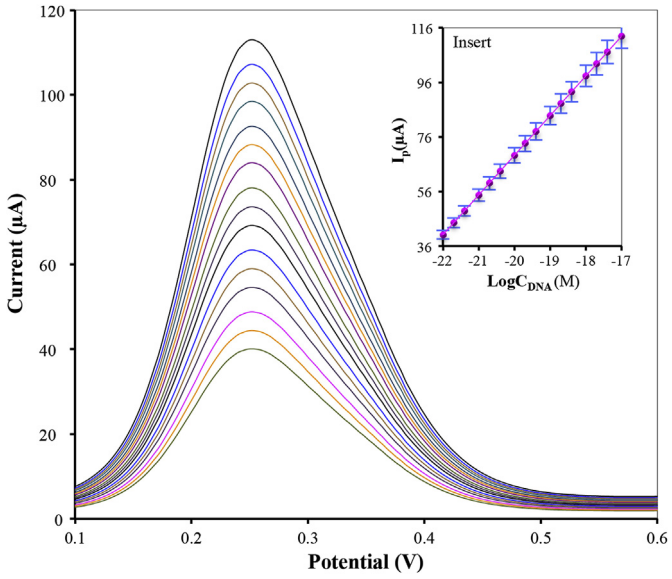

Fig. 7. DPV curves of the hybridized ssDNA-biosensor with target DNA of 1×10^{-22}, 2×10^{-22}, 4×10^{-22}, 1×10^{-21}, 2×10^{-21}, 4×10^{-21}, 1×10^{-20}, 2×10^{-20}, 4×10^{-20}, 1×10^{-19}, 2×10^{-19}, 4×10^{-19}, 1×10^{-18}, 2×10^{-18}, 4×10^{-18} and 1×10^{-17} M in a 1 mM of $K_4Fe(CN)_6$ in the PBS (from top to bottom). Insert: The relationship between the peak current (I_p) and Log (target DNA). The DPV parameters were set to a scan rate of 4 mV s^{-1}, 50 mV pulse amplitude, 20 ms pulse width and −0.2 v initial potential.

weeks, it retained the significant results of its initial response, indicating a good stability. To test the reproducibility of ssDNA-biosensor batch production, 25 ssDNA-biosensors were made by using the same AuPd NWs/D-GQDs-GMA, probe DNA and preparation procedure. After hybridized with target DNA of 1.0×10^{-21} M, their DPV responses were measured in the PBS of pH 7. Relative standard deviation (RSD%) of the DPV responses is about 2.4%, indicating a high reproducibility. For the same ssDNA-biosensor, it was used for successive detection of 1.0×10^{-21} M target DNA. For the each detection, the ssDNA-biosensor was hybridized with target DNA and then carried out the DPV measurement. After that, the hybridized ssDNA-biosensor was immersed in a 50 mM NaOH aqueous solution for 1 min and washed with the PBS of 7 to remove the target DNA from the electrode surface. The regenerated ssDNA-biosensor was used for the next detection. The RSD of ssDNA-biosensor in 30 successive target DNA detection is 1.9%. This illustrates the reproducible characteristic of ssDNA-biosensor.

The anti-interference is significant parameter of the biosensor for detection of DNA in biological conditions. To test the selectivity and the specific hybridization process, DPV behaviours of the hybridized ssDNA biosensors with complementary DNA, single mismatch DNA and non-complementary DNA were investigated in a 1 mM of $Fe(CN)_6^{4-}$ in the PBS. Fig. s9 indicates that the hybridized ssDNA-biosensor with complimentary DNA offers the most sensitive DPV response towards $Fe(CN)_6^{4-}$. This is because "molecular beacon"-like probe DNA was attached to the AuPd NW surface to form a stem-loop structure by self-assembling via gold-thiol bonding. The actual hybrid sequence is situated in the loop part of the single strand, and the stem is formed by base paring two complementary arm sequences at either side of the loop. If the complimentary DNA (target DNA) is absent, the stem-loop probe is "closed". The standing ssDNA on the AuPd NW surface is difficult to well interact with sensing materials to form stable bioconjugate. This greatly restricts to trigger the DNA conductivity and results in a relatively low DPV response towards $Fe(CN)_6^{4-}$. On the hybridization with target DNA the conformation undergoes a thermodynamically driven change to an "open" structure and finally form a thermodynamically stable dsDNA. The dsDNA can strongly interact with the sensing materials to form stable bioconjugate and achieves to trigger the DNA conductivity via the overlapping π-electron systems, leading to an enhanced DPV response towards $Fe(CN)_6^{3-/4-}$. Hence, the hybridization of probe DNA with target DNA brings an obvious increase in the DPV signal. However, the change become very weak if the target DNA was replaced by single mismatch DNA or non-complementary DNA. Because the base pairs do not completely match between the probe DNA and single mismatch DNA or non-complementary DNA, their hybridization can not form dsDNA via the regular base pairing. Owing to the failure in striggering DNA conductivity, the presence of single

Table 1
Comparison of the DNA biosensor for electrochemical detection of DNA.

Electrode	Technique	Linear range	LOD	Ref.
Aminobenzo-18-crown-6-Cu(II)/molecule beacon	DPV	1×10^{-13}-5×10^{-13} M	6×10^{-14} M	[10]
Carboxyl functionalized Fe_3O_4-glucosyltransferase	DPV	5×10^{-10}-9×10^{-8} M	1.4×10^{-10} M	[11]
Nitrogen-doped multiple graphene aerogel/gold nanostar	DPV	1×10^{-21}-1×10^{-16} g ml^{-1}	3.9×10^{-22} g ml^{-1}	[23]
Effective T junction induced transcription amplification	DPV	5×10^{-15}-5×10^{-9} M	4×10^{-16} M	[35]
MS_2/multi-walled carbon nanotube/Au nanoparticles	DPV	1×10^{-12}-5×10^{-8} M	2.5×10^{-15} M	[36]
Molecular beacon mediated circular strand displacement polymerization and hyperbranched rolling circle amplification	DPV	1×10^{-17}-1×10^{-11} M	8.9×10^{-18} M	[14]
Hairpin	DPV	2.5×10^{-11}-2.5×10^{-8}M	2×10^{-11} M	[37]
Sulfonated polyaniline-graphene oxide	DPV	1×10^{-14}-1×10^{-6} M	3.06×10^{-15} M	[38]
Tetramethylbenzidine sulfate-peroxidase	Amperometric method	1×10^{-15}-1×10^{-10} M	4×10^{-16} M	[13]
Gold nanotubes	DPV	1×10^{-15}-1×10^{-13} g l^{-1}	1×10^{-17} g l^{-1}	[39]
Multilayer graphene-gold nanocomposite	DPV	1×10^{-13}-1×10^{-16} M	4.1×10^{-17} M	[40]
AuPd NWs/D-GQDs-GMA	DPV	1×10^{-22}-1×10^{-17} M	4.7×10^{-23} M	Present work

mismatch DNA and non-complementary DNA only produces a small change in the DPV signal. The above results verify that the proposed ssDNA-biosensor is of good selectivity for detection of target DNA.

3.7. Sample analysis

The feasibility of newly developed DNA biosensor for possible applications was investigated by analyzing peanut milk beverage. The DNA biosensor was firstly hybridized with target DNA in the extract of a peanut milk beverage, and then DPV response of the sensor was measured in a 1.0 mM $K_4Fe(CN)_6$ in the PBS of pH 7. In addition, the spike and recovery experiments were performed by hybridizing with the target DNA in which the known concentrations of peanut allergen-Ara h 1 were added and then measuring the DPV response towards $Fe(CN)_6^{4-}$. The result was that the concentration of peanut allergen-Ara h 1 in the peanut milk beverage was 2.42×10^{-15} M, and the recovery of peanut allergen-Ara h 1 for the spiked samples analysis was 96.7%. These implied that the proposed DNA-biosensor could be used to detect the peanut allergen in actual samples.

4. Conclusions

The study demonstrated the synthesis of gold-palladium nanowaxberries/dodecylamine-functionalized graphene quantum dots-graphene micro-aerogel ans its application as an electrochemical sensing platform for detection of peanut allergen-Ara h 1. The hybrid of graphene micro-aerogel, dodecylamine-functionalized graphene quantum dots and gold-palladium nanowaxberries greatly improve the electron/ion conductivity and specific surface area. The as-prepared composite exhibits high electrochemical activity towards $Fe(CN)_6^{4-}$. DNA biosensor based on the composite has a better sensitivity for the electrochemical detection of peanut allergen Ara h 1 compared with all reported DNA biosensors. The study also opens a window on the electronic properties of graphene aerogel, graphene quantum dots and noble metal nanoparticles as well their hybrids to meet the needs of further uses as an electrochemical platform in electrochemical sensors and electrocatalysis.

Acknowledgements

The authors acknowledge the financial support from the National Natural Science Foundation of China (No. 21576115) and MOE & SAFEA for the 111 Project (B13025).

Appendix A. Supplementary data

Supplementary data related to this article can be found at https://doi.org/10.1016/j.aca.2018.01.031.

References

[1] C. Bindslev-Jensen, D. Briggs, M. Osterballe, Can we determine a threshold level for allergenic foods by statistical analysis of published data in the literature, Allergy 57 (2002) 741–745.
[2] S.A. Bock, A. Muñoz-Furlong, H.A. Sampson, Fatalities due to anaphylactic reactions to foods, J. Allergy Clin. Immunol. 107 (2001) 191–193.
[3] C. Mcvey, F. Huang, C. Elliott, C. Cao, Endonuclease controlled aggregation of gold nanoparticles for the ultrasensitive detection of pathogenic bacterial DNA, Biosens. Bioelectron. 92 (2017) 502–508.
[4] Q. Liu, C. Ma, X. Liu, Y. Wei, C. Mao, J. Zhu, A novel electrochemiluminescence biosensor for the detection of microRNAs based on a DNA functionalized nitrogen doped carbon quantum dots as signal enhancers, Biosens. Bioelectron. 92 (2017) 273–279.
[5] K. Faulds, W.E. Smith, D. Graham, DNA detection by surface enhanced resonance Raman scattering (SERRS), Analyst 130 (2005) 1125–1131.
[6] Y. Miao, J. Lv, G. Yan, Hybrid detection of target sequence DNA based on phosphorescence resonance energy transfer, Biosens. Bioelectron. 94 (2017) 263–270.
[7] L. Liu, C. Wu, S. Zhang, Ultrasensitive detection of DNA and Ramos cell using in situ selective crystallization based quartz crystal microbalance, Anal. Chem. 89 (2017) 4309–4313.
[8] W. Chen, X. Fang, H. Li, H. Cao, J. Kong, DNA-mediated inhibition of peroxidase-like activities on platinum nanoparticles for simple and rapid colorimetric detection of nucleic acids, Biosens. Bioelectron. 94 (2017) 169–175.
[9] H.W. Zhou, G.D. Wang, D.L. Xie, B. Cai, Y.M. Liu, X.Z. Zhao, Au nanoparticles enhanced fluorescence detection of DNA hybridization in picoliter microfluidic droplets, Biomed. Microdevices 16 (2014) 479–485.
[10] F. Zhan, X. Liao, F. Gao, W. Qiu, Q. Wang, Electroactive crown ester-Cu(2+) complex with in-situ modification at molecular beacon probe serving as a facile electrochemical DNA biosensor for the detection of CaMV 35s, Biosens. Bioelectron. 92 (2016) 589–595.
[11] H. Yin, Z. Yang, H. Wang, Y. Zhou, S. Ai, Electrochemical biosensor for hydroxymethylated DNA detection and β-glucosyltransferase activity assay based on enzymatic catalysis triggering signal amplification, Sensor. Actuator. B Chem. 243 (2017) 602–608.
[12] A. Benvidi, S. Jahanbani, Self-assembled monolayer of SH-DNA strand on a magnetic bar carbon paste electrode modified with Fe_3O_4@Ag nanoparticles for detection of breast cancer mutation, J. Electroanal. Chem. 768 (2016) 47–54.
[13] L. Jia, S. Shi, R. Ma, W. Jia, H. Wang, Highly sensitive electrochemical biosensor based on nonlinear hybridization chain reaction for DNA detection, Biosens. Bioelectron. 80 (2016) 392–397.
[14] X. Li, J. Guo, Q. Zhai, J. Xia, G. Yi, Ultrasensitive electrochemical biosensor for specific detection of DNA based on molecular beacon mediated circular strand displacement polymerization and hyperbranched rolling circle amplification, Anal. Chim. Acta 934 (2016) 52–58.
[15] E.J.H. Wee, M.J.A. Shiddiky, M.A. Brown, M. Trau, eLCR: electrochemical detection of single DNA base changes via ligase chain reaction, Chem. Commun. 48 (2012) 12014–12016.
[16] P. Miao, B. Wang, F. Meng, J. Yin, Y. Tang, Ultrasensitive detection of MicroRNA through rolling circle amplification on a DNA tetrahedron decorated electrode, Bioconjugate Chem. 26 (2015) 602–607.
[17] Y. Kuzin, A. Porfireva, V. Stepanova, V. Evtugyn, I. Stoikov, G. Evtugyn, T. Hianik, Impedimetric detection of DNA damage with the sensor based on silver nanoparticles and neutral red, Electroanalysis 27 (2016) 2800–2808.
[18] H. Pan, H. Yu, N. Wang, Z. Zhang, G.C. Wan, H. Liu, X. Guan, D. Chang, Electrochemical DNA biosensor based on a glassy carbon electrode modified with gold nanoparticles and graphene for sensitive determination of Klebsiella pneumoniae carbapenemase, J. Biotechnol. 214 (2015) 133–138.
[19] M. Pacios, N. Yilmaz, I. Martin-Fernandez, R. Villa, P. Godignon, M. Del Valle, J. Bartroli, M.J. Esplandiu, A simple approach for DNA detection on carbon nanotube microelectrode arrays, Sensor. Actuator. B Chem. B162 (2012) 120–127.
[20] L. Zhu, L. Luo, Z. Wang, DNA electrochemical biosensor based on thionine-graphene nanocomposite, Biosens. Bioelectron. 35 (2012) 507–511.
[21] C. Liu, D. Jiang, G. Xiang, L. Liu, F. Liu, X. Pu, An electrochemical DNA biosensor for the detection of Mycobacterium tuberculosis, based on signal amplification of graphene and a gold nanoparticle- polyaniline nanocomposite, Analyst 139 (2014) 5460–5465.
[22] H. Bei, R. Li, Z. Li, J. Liu, Z. Gu, G. Wang, Fabrication of a high density graphene aerogel–gold nanostar hybrid and its application for the electrochemical detection of hydroquinone and o-dihydroxybenzene, RSC Adv. 5 (2015) 54211–54219.
[23] R. Li, L. Liu, H. Bei, Z. Li, Nitrogen-doped multiple graphene aerogel/gold nanostar as the electrochemical sensing platform for ultrasensitive detection of circulating free DNA in human serum, Biosens. Bioelectron. 79 (2016) 457–466.
[24] J.W.S. Hummers, E.O. Richard, The preparation of graphite oxide, J. Am. Chem. Soc. 80 (1958) 1339.
[25] R.Y. Li, J. Chen, X.Y. Zhou, Z.J. Li, J.K. Liu, Fabrication of zinc–histidine-functionalized graphene quantum dot framework amphiphilic nanoparticles and application in the synthesis of polystyrene microspheres for adsorption of Cu2+ by Pickering emulsion polymerization, RSC Adv. 6 (2016) 102534–102541.
[26] X. Zhou, R.Y. Li, Z.J. Li, J. Liu, Z. Gu, G. Wang, A surface-enhanced Raman scattering strategy for detection of peanut allergen ara h 1 using a bipyramid-shaped gold nanocrystal substrate with an improved synthesis, RSC Adv. 4 (2014) 15363–15370.
[27] N.E. Walczyk, P.M.C. Smith, E.R. Tovey, T.H. Roberts, Peanut protein extraction conditions strongly influence yield of allergens Ara h 1 and 2 and sensitivity of immunoassays, Food Chem. 221 (2017) 335–344.
[28] S. Tongay, T. Schumann, X. Miao, B.R. Appleton, A.F. Hebard, Tuning Schottky diodes at the many-layer- graphene/semiconductor interface by doping, Carbon 49 (2011) 2033–2038.
[29] Y.R. Yan, Q.T. Huang, C. Wei, S.R. Hu, H.Q. Zhang, W.X. Zhang, W.Z. Yang, P.H. Dong, M.L. Zhu, Z.M. Wang, Microwave-assisted synthesis of carbon dots–zinc oxide/multi-walled carbon nanotubes and their application in electrochemical sensors for the simultaneous determination of hydroquinone and catechol, RSC Adv. 6 (2016) 115317–115325.
[30] E. Laviron, General expression of the linear potential sweep voltammogram in

the case of diffusionless electrochemical systems, J. Electroanal. Chem. Interfacial Electrochem. 101 (1979) 19–28.
[31] F.C. Anson, Application of potentiostatic current integration to the study of the adsorption of cobalt(III)-(ethylenedinitrilo(tetraacetate)) on mercury electrodes, Anal. Chem. 36 (1964) 313–315.
[32] K.H. Koh, S.H. Noh, T.H. Kim, W.J. Lee, S.C. Yi, T.H. Han, A graphene quantum dot/phthalocyanine conjugate: a synergistic catalyst for the oxygen reduction reaction, RSC Adv. 7 (2017) 26113–26119.
[33] M.D. Levi, D. Aurbach, Simultaneous measurements and modeling of the electrochemical impedance and the cyclic voltammetric characteristics of graphite electrodes doped with lithium, J. Phys. Chem. B 101 (1997) 4630–4640.
[34] D.T. Odom, E.A. Dill, J.K. Barton, Robust charge transport in DNA double crossover assemblies, Chem. Biol. 7 (2000) 475–478.
[35] R. Yuan, S.J. Ding, Y.R. Yan, Y. Zhang, Y.H. Zhang, W. Cheng, A facile and pragmatic electrochemical biosensing strategy for ultrasensitive detection of DNA in real sample based on defective T junction induced transcription amplification, Biosens. Bioelectron. 77 (2016) 19–25.
[36] X. Liu, H.L. Shuai, Y.J. Liu, K.J. Huang, An electrochemical biosensor for DNA detection based on tungsten disulfide/multi-walled carbon nanotube composites and hybridization chain reaction amplification, Sensor. Actuator. B Chem. 235 (2016) 603–613.
[37] C.L. Zhong, G. Yang, N. Wang, F.H. Ji, Y. Zhang, X.J. Ding, J.H. Yang, J. Zhang, Hairpin assembly amplified electrochemical biosensor for highly sensitive and specific detection of DNA, Electroanalysis 28 (2016) 1578–1583.
[38] L. Meng, H.Y. Chen, T. Ge, T. Yang, K. Jiao, Sulfonated polyaniline-graphene oxide hybrids: synthesis and effect of monomer composition on the electrochemical signal for direct DNA detection, J. Polym. Sci. Part A Polym. Chem. 54 (2016) 1762–1773.
[39] R. Torati, V. Reddy, S.S. Yoon, C. Kim, Electrochemical biosensor for Mycobacterium tuberculosis, DNA detection based on gold nanotubes array electrode platform, Biosens. Bioelectron. 78 (2016) 483–488.
[40] X.L. Sun, M. Jia, L. Guan, J. Ji, Y.Z. Zhang, L.L. Tang, Z.J. Li, Multilayer graphene-gold nanocomposite modified stem-loop DNA biosensor for peanut allergen-Ara h1 detection, Food Chem. 172 (2015) 335–342.